



Faraday instability of a liquid layer in ultrasonic atomizationSongmei Yuan ^{*}, Yu Zhang , and Yang Gao*School of Mechanical Engineering, Beihang University, No. 37, Xueyuan Road, Beijing 100191, China*

(Received 25 September 2021; accepted 23 February 2022; published 16 March 2022)

Ultrasonic atomization is increasingly used in industry; however, the lack of corresponding theoretical studies on the atomization mechanism and performance effects has led to a lack of scientific application. In this study, multiple Faraday waves in ultrasonic atomization were simulated and a comparative study of Faraday instability theory was conducted in conjunction with experiments. For the inviscid case, the parametric curve equations explain the excitation and competition mechanisms of different frequency harmonics. The position of the parameter pair determines whether the perturbation of the Faraday wave is linear or not. The surface perturbation displacements of Faraday waves are plotted from theoretical, experimental, and simulation perspectives, respectively, and the three agree well. Different parameters correspond to different parameter curve positions and maximum perturbation growth rates, which determine the intensity of the Faraday instability and thus cause changes in the atomization characteristics. In the viscous case, the Faraday instability depends on the wave number and viscosity, and the intensity of the instability can be obtained from the instability threshold. All the theoretical predictions in this study are validated by experiments and simulations, which can provide scientific guidance for process optimization of practical ultrasonic atomization production.

DOI: [10.1103/PhysRevFluids.7.033902](https://doi.org/10.1103/PhysRevFluids.7.033902)**I. INTRODUCTION**

When a periodic vibration is applied perpendicular to the fluid, surface standing waves can be observed at the interface of different fluid layers, where the surface waves vibrate at half the excitation frequency. Faraday first discovered this phenomenon experimentally, so these surface waves were called “Faraday waves” [1]. The appearance of Faraday waves aroused the interest of researchers in the corresponding physical-mathematical models, which led to the Faraday instability problem. Benjamin and Ursell first analyzed the Faraday instability of an ideal fluid theoretically [2]. Based on the assumptions of linearity and being viscosity free, a standard Mathieu equation was proposed to describe the development of Faraday wave amplitudes on the surface of a horizontal fluid. According to their theory, harmonics of all frequencies appear with the same probability. Eisenmenger [3] and Ciliberto and Gollub [4] added a linear damping term to the Mathieu equation and explained the effect of viscosity on Faraday instability utilizing a phenomenological model. Based on Floquet’s linear stability analysis method, Kumar and Tuckerman [5] and Kumar [6] transformed the effect of viscosity on Faraday instability into an eigenvalue problem, solved to obtain the acceleration amplitude threshold, and explained the experimentally more likely occurrence of subharmonics. Zhang and Viñals derived the governing equation for Faraday wave amplitude based on liquid viscosity and vibration angular frequency conditions; the corresponding Faraday wave modes can be predicted [7].

*yuansmbuaa@163.com

In addition, experimental studies of Faraday instability have been extensively carried out. The interaction of different Faraday wave modes is a very interesting nonlinear phenomenon in Faraday instability. When the inertial force exceeds a threshold, various modes of Faraday waves appear on the liquid surface. Bosch *et al.* observed square Faraday waves and found that the maximum fluctuation amplitude tends to be located at the square nodes when the potential energy is at its lowest [8]. Kityk *et al.* photographed square, hexagonal, and bar Faraday waves using optical absorption techniques and explained the generation of these waves using spectral analysis methods [9]. Christiansen *et al.* generated ordered capillary and quasicrystalline waves from three and four planar standing waves [10]. Kumar and Bajaj experimentally observed the competition between different Faraday wave modes, including equilateral triangular, hexagonal, striped, and square Faraday waves, and found that viscosity, amplitude, and frequency conditions determine the different modes [11].

In addition to theoretical derivation and experimental investigation, a large number of studies have performed nonlinear numerical simulations of Faraday instabilities using finite element methods. Périnet *et al.* analyzed the dynamics of Faraday waves by three-dimensional numerical simulations, and obtained hexagonal and square Faraday waves [12,13], which are consistent with the experimental phenomena of Kityk *et al.* [9]. Li *et al.* studied single-mode Faraday instability with detailed interfacial dynamics by three-dimensional simulations and elucidated the mechanism of ligament formation and rupture [14]. Most other studies have focused on solving the two-dimensional Navier-Stokes equations; for example, Takagi and Matsumoto studied nonlinear plume formation at the two-phase flow interface by numerical simulations and verified the feasibility of the phase-field approach [15].

Faraday instability has gained widespread attention not only in academia, but also in industrial and biomedical manufacturing fields, where atomization of liquids using the Faraday instability principle has been widely applied [16–20], and one of the most typical liquid atomization methods is ultrasonic atomization. Compared with other traditional atomization methods, ultrasonic atomization is more popular because of its environmental friendliness, high efficiency, and uniform droplet size [21,22]. During ultrasonic atomization, vertical sinusoidal vibrations at ultrasonic frequencies (>20 kHz) are applied to the liquid, resulting in atomization, which was first observed by Wood *et al.* in 1927 [23]. Lang visualized Faraday waves on the liquid surface during ultrasonic atomization and summarized an empirical formula for the average droplet diameter [24]. Later, Rajan and Pandit proposed the use of dimensionless quantities such as the Weber number (N_{We}), Ohnesorge number (N_{Oh}), and intensity number (N_{In}) to explain the effect of different physicochemical properties on droplet size [25]. Wilkes and Basaran performed a two-dimensional simulation of the rupture process of a pendant droplet under forced vibration and investigated the effects of different parameters (amplitude, frequency, droplet properties, droplet size, and rod position) on this process, showing that the timescales on which these parameters enter lead to differences in the final droplet ejection volume [26,27].

In summary, most of the studies have used the theory of Faraday instability to explain the interface deformation, but they have not been elaborated upon in comparison with the ultrasonic atomization phenomenon. In addition, there is a lack of relevant theoretical studies on the influence mechanism of atomization properties, which leads to some disconnection between theoretical studies and practical applications. In this paper, the evolution of multiple Faraday waves in ultrasonic atomization is simulated, and the instability theory is analyzed in comparison with the experiments. Parametric curve equations are derived, and the mechanism of Faraday wave evolution in ultrasonic atomization is explained in combination with experiments and simulations. In particular, the mechanism of parameter influence on atomization characteristics is comprehensively discussed based on practical application requirements.

The contents of this paper are organized as follows. In the next section, the experimental setup is described. In Sec. III, the physical model corresponding to ultrasonic atomization is established and the dispersion relation is given. In Sec. IV, the numerical simulation method is described and the grid size is chosen. In Sec. V, for the inviscid case, we use instability theory to obtain the parameter

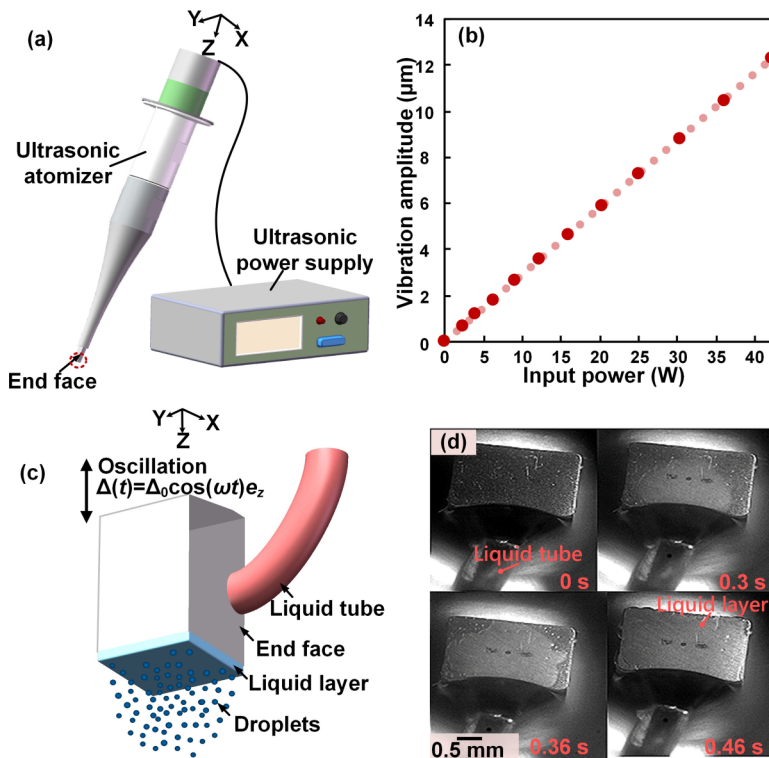


FIG. 1. (a) Schematic of ultrasonic atomization system. (b) Variation of vibration amplitude with input power. (c) Enlarged view of the end face of the atomizer [in the red dashed circle in (a)]. (d) The formation process of the liquid layer on the lower end face.

curve equation and describe quantitatively the surface disturbance displacement of Faraday waves through experiments and simulations. For the viscous case, the conditions of Faraday instability are analyzed qualitatively. In Sec. VI, the effects of different parameters (amplitude, frequency, liquid surface tension, liquid density, liquid depth, and viscosity) on Faraday instability are predicted using parameter curves and instability thresholds, and the related atomization characteristics are investigated by experiments and simulations, and the theoretical results are verified. Section VII summarizes the Conclusions of this study.

II. EXPERIMENT

Figure 1(a) shows the ultrasonic atomizer system used in this study, which consists of an atomizer nozzle (CAT-35 ILDS series, USI) and an ultrasonic power supply [22]. The atomizer nozzle uses the electrostrictive effect to convert the electrical energy into sinusoidal vibrations in the z direction. The vibration displacement expression is

$$\Delta(t) = \Delta_0 \cos(\omega t) e_z, \quad (1)$$

where Δ_0 is the oscillation acceleration amplitude, ω is the angular frequency of vibration, and e_z is the unit vector along the z axis direction in the Cartesian coordinate system, namely, $e_z = (0, 1)$. By adjusting the electrical parameters, the vibration frequency f can be set to 36, 45, 60, and 80 kHz. In addition, the vibration amplitude can be changed by adjusting the input power. Figure 1(b) shows the corresponding vibration amplitude for different input powers, which was measured by a laser Doppler vibrometer (Polytec OFV534/5000, Germany). The amplitude increases proportionally as

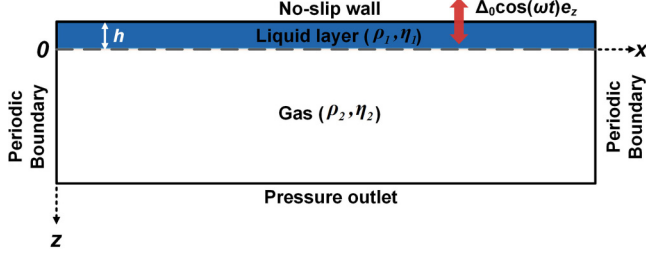


FIG. 2. Physical model.

the input power increases. Figure 1(c) shows a magnified view of the end face [inside the red dashed circle in Fig. 1(a)] and Fig. 1(d) shows in detail the formation process of the liquid layer on the end face. The liquid flows through the supply tube to the side of the vibrating head and subsequently flows to the bottom of the end face. After a period of spreading, a liquid layer gradually formed. In the experiments, the liquid flow rate was fixed at $1 \mu\text{l}/\text{min}$.

To ensure the statistical significance of the experimental results, all experiments in this paper were repeated no less than five times.

III. GOVERNING EQUATIONS AND DISPERSION RELATIONS

According to Fig. 1(c), we consider the liquid layer (depth h) on the end face of the vibrating head and build a physical model as shown in Fig. 2. The whole fluid system is governed by the incompressible and immiscible viscous Navier-Stokes equations:

$$\rho \left[\frac{\partial \mathbf{u}}{\partial t} + (\mathbf{u} \cdot \nabla \mathbf{u}) \right] = -\nabla P + \rho \mathbf{G} + \nabla \cdot \eta (\nabla \mathbf{u} + \nabla \mathbf{u}^T) + \mathbf{F}_s, \quad (2)$$

$$\nabla \cdot \mathbf{u} = 0, \quad (3)$$

where \mathbf{u} is the velocity vector, P is the pressure, and \mathbf{G} is the superimposed value of the acceleration of gravity and the acceleration of the periodic oscillation, which can be written as

$$\mathbf{G} = [g + A_0 \cos(\omega t)] \mathbf{e}_z. \quad (4)$$

The surface tension force \mathbf{F}_s in the continuum surface force (CSF) model is given by

$$\mathbf{F}_s = \sigma \kappa \nabla H_\varepsilon, \quad (5)$$

where σ is the surface tension, κ is the curvature, and H_ε is the smoothed Heaviside function with thickness ε . The surface tension is converted into volume force and is dispersed near the interface.

The initially flat, stationary two-dimensional interface position between the two fluids (the dashed line in Fig. 2) is defined by $z = 0$. When the interface is disturbed, we define $z = \zeta(x, t) = \xi(t) e^{ikx}$ as the function of the interface position, where k is the wave number and $\xi(t)$ is the time-dependent part of $\zeta(x, t)$.

The kinematic condition at the interface of the two fluids is given by

$$\frac{\partial \zeta}{\partial x} + (\mathbf{u}_j \cdot \nabla) \zeta = \mathbf{u}_{j|z=\zeta}, \quad (6)$$

where subscript $j = 1, 2$ denotes different layers of fluids.

The density and viscosity of the lower and the upper layers of fluids are written as a function of z :

$$(\rho, \eta) = \begin{cases} (\rho_1, \eta_1) & z < \zeta(x, t) \\ (\rho_1, \eta_2) & z > \zeta(x, t) \end{cases}, \quad (7)$$

and $\rho_1 > \rho_2$.

Neglecting the nonlinear velocity term as well as the surface tension force term in Eqs. (2) and (3), we obtain the linearized governing equations as follows [28]:

$$\rho \frac{\partial \mathbf{u}}{\partial t} = -\nabla P + \rho \mathbf{G} + \nabla \cdot \eta(\nabla \mathbf{u} + \nabla \mathbf{u}^T), \quad (8)$$

$$\nabla \cdot \mathbf{u} = 0. \quad (9)$$

The linearized governing equations of displacement disturbance $\xi(t)$ can then derive a Mathieu equation with a damping term β using the method proposed by Benjamin and Ursell [2]:

$$\frac{d^2 \xi}{dt^2} + 2\beta \frac{d\xi}{dt} + (a - 2q \cos \omega t)\xi = 0, \quad (10)$$

where

$$\beta = 2k^2 \frac{\eta_1 + \eta_2}{\rho_1 + \rho_2}, \quad (11)$$

$$a = \frac{\sigma k^3 + (\rho_1 - \rho_2)gk}{\rho_1 + \rho_2}, \quad (12)$$

and

$$q = \frac{(\rho_1 - \rho_2)kA_0}{2(\rho_1 + \rho_2)}. \quad (13)$$

The dispersion relation of the angular frequency Ω of freely vibrating surface waves and the wave number k is obtained as follows:

$$\Omega^2 = \frac{\sigma k^3 + (\rho_1 - \rho_2)gk}{\rho_1 + \rho_2}. \quad (14)$$

According to the Floquet theory [29,30], $\xi(t)$ can be written in the Floquet form as

$$\xi(t) = e^{(\gamma + i\alpha)t} \sum_n \xi_n(k) e^{in\omega t}, \quad (15)$$

where $\gamma + i\alpha$ is the Floquet exponent, and ξ_n is the coefficient of Floquet modes n .

We substitute Eq. (15) into Eq. (10), and obtain the recursion relation:

$$(\delta^2 + 2\beta\delta + a)\xi_n = q(\xi_{n+1} + \xi_{n-1}), \quad (16)$$

where $\delta = \gamma + i(\alpha + n\omega)$. Setting $\gamma = 0$ and $q = 0$, the resonance condition can be obtained by solving the nontrivial solution to Eq. (16).

$$a^{1/2} = \frac{1}{2}l\omega = \Omega, \quad (17)$$

where l is even for harmonic cases and odd for subharmonic cases. This resonance condition can also be considered as an implicit dispersion relation.

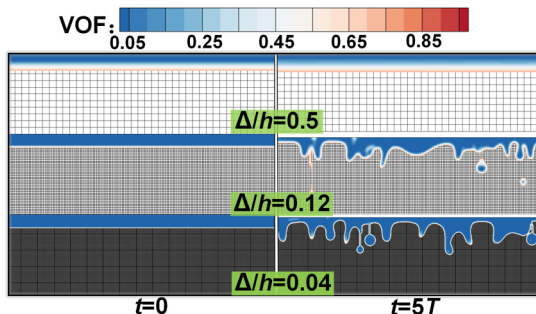


FIG. 3. Visualization of the gas-liquid interface deformation at different grid resolutions (Δ is the grid size and T is the vibration period).

IV. NUMERICAL METHODS AND GRID SELECTION

To simulate the liquid deformation as realistically as possible without adding excessive time cost, we chose to calculate about ten surface waves. We roughly estimated the wavelength λ using Kelvin's formula [31]: $\lambda = (8\pi\sigma/\rho f^2)^{1/3}$. The wavelength λ increases as the vibration frequency f decreases, and for our atomizer, the wavelength is maximum when the vibration frequency is 36 kHz. Considering that de-ionized water is the most commonly used atomization object, we substitute the surface tension and density of de-ionized water into Kelvin's formula and calculate the corresponding wavelength to be about $112.18 \mu\text{m}$. Therefore, it is appropriate to set the model length to 1 mm. According to the experimental conditions, the liquid depth h range is $20\text{--}130 \mu\text{m}$, and the height of the gas phase is set to be about 1.5 times the maximum liquid-phase depth; therefore, the whole model height is set to 0.3 mm. The upper boundary of the liquid layer is a no-slip wall, which is set by the user-defined function (UDF) in the harmonic motion form. To be consistent with the experimental conditions, the gas-liquid interface is initially located at $z = 0$, the bottom of the gas phase is the pressure outlet, and the left and right boundaries are periodic. A uniformly staggered grid is used to discretize the governing equations [32]. Coupled level sets (LSs) and volume functions of fluid (VOF) are used to capture the deformation of surface waves [33]. This method has been applied to many complex two-phase flow problems due to the curvature continuity property of the LSs and the absolute mass conservation of the VOF [34].

In numerical simulations, it is necessary to compare the solution accuracy and cost for different grid resolutions and to select the optimal grid size. We choose three different grid resolutions ($\Delta/h = 0.5, 0.12, 0.04$) to compare the accuracy of the gas-liquid interface deformation at the initial state ($t = 0$) and the fifth vibration cycle ($t = 5T$), as shown in Fig. 3. The value of VOF represents the volume fraction occupied by the gas. For better display, the color of the pure gas phase is hidden in Fig. 3. When $\Delta/h = 0.5$, the gas-liquid interface is very blurred and the liquid profile hardly changes at $t = 5T$, which is due to the grid size exceeding the liquid deformation. When $\Delta/h = 0.12$, the gas-liquid interface becomes clear and the change of the liquid-phase profile at $t = 5T$ can be shown. However, the droplet profile resolution is low, which deteriorates the accuracy of the droplet size measurement. When $\Delta/h = 0.04$, the clarity of both the gas-liquid interface and the droplet profile is high, which satisfies the requirements of our study. Also, the computational cost is within the affordable range; therefore, we choose this grid refinement level in the subsequent simulations.

V. EVOLUTIONARY MECHANISM OF FARADAY WAVES

A. Inviscid case

When the atomizer starts to vibrate for 0.01 s, the Faraday wave on the liquid surface is shown in Fig. 4, where $f = 36 \text{ kHz}$, $\Delta_0 = 3.7 \mu\text{m}$, and the atomization object is de-ionized water. The liquid

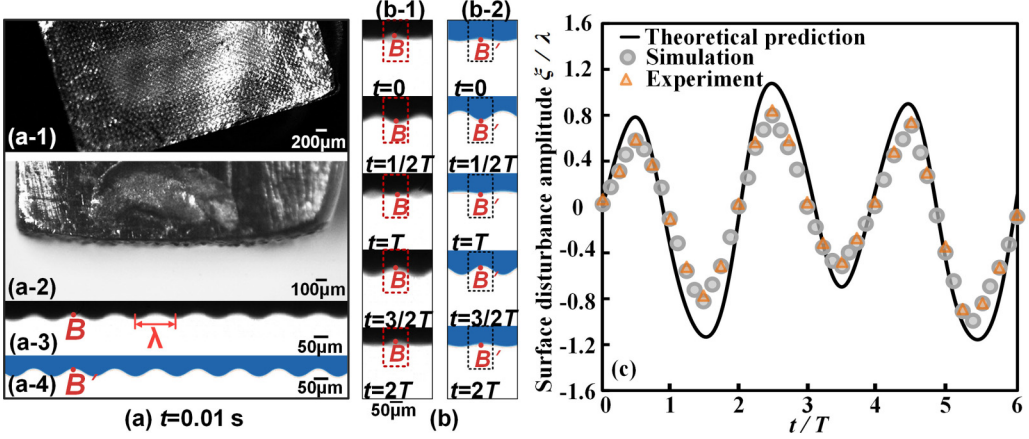


FIG. 4. (a) Faraday wave image at $t = 0.01$ s. (b) The position change of point B (in the experiment) and point B' (in the simulation) during two vibration periods. (c) Evolution of the perturbation displacement of the Faraday wave according to the theoretical, experimental, and simulation results. The horizontal and vertical coordinates represent the dimensionless forms of the time and surface perturbation displacements, respectively, and the vibration period T and wavelength λ are used for creating the dimensionlessness. The detailed photographic parameters and displacement measurements are in Appendix A.

layer evolves uniform Faraday waves [Fig. 4(a-1)], consisting of a regular arrangement of crests and troughs [Figs. 4(a-2) and 4(a-3)], which indicates that the Faraday waves are in a steady state. The same Faraday waves are also observed in the simulation [Fig. 4(a-4)]. Point B [Fig. 4(a-3)] and point B' [Fig. 4(a-4)] in the experiment and simulation were selected, and the displacement changes of these two points in two vibration periods were observed continuously; the results are shown in Figs. 4(b) and 4(c). At the same moment, these two points are located at the same position and the fluctuation form of the Faraday wave is a sinusoidal-like function. Within $2T$, the wave crest and trough alternated once, indicating that the fluctuation frequency of the Faraday wave is half of the vibration frequency.

At $t = 0.03$ s, the Faraday wave gradually becomes turbulent [Fig. 5(a-1)], accompanied by the droplet generation, and atomization occurs [Figs. 5(a-2) and 5(a-3)], indicating that the Faraday wave evolves from a steady state to an unsteady state. In the simulation, the liquid also undergoes atomization [Fig. 5(a-4)]. We observed the generation process of these droplets, one of which is illustrated in Fig. 5(b). We chose the bottom point of this droplet (points C and C') and measured the displacement change at this point, as in Fig. 5(c). The droplet formation process in the experiment and simulation is similar: The crest of the Faraday wave first elongates into a small protrusion, after which it undergoes refraction and reelongation, the cross-sectional area of the protrusion shrinks, and after about $4T$, the protrusion breaks due to the capillary pinch mechanism and a droplet is formed.

Based on the Faraday wave evolution in Figs. 4 and 5, we try to explain it by instability theory. The viscosity of de-ionized water is low, and to simplify the study, we assume that $\eta_1 = \eta_2 = 0$ and the damping term β in Eq. (10) can be neglected. Defining $\tau = \omega t/2$, we obtain the following dimensionless Mathieu equation:

$$\frac{d^2\xi}{d\tau^2} + (a^* - 2q^* \cos 2\tau)\xi = 0, \quad (18)$$

with definitions of

$$a^* = \frac{4}{\omega^2} \frac{\sigma k^3 + (\rho_1 - \rho_2)gk}{\rho_1 + \rho_2}, \quad (19)$$

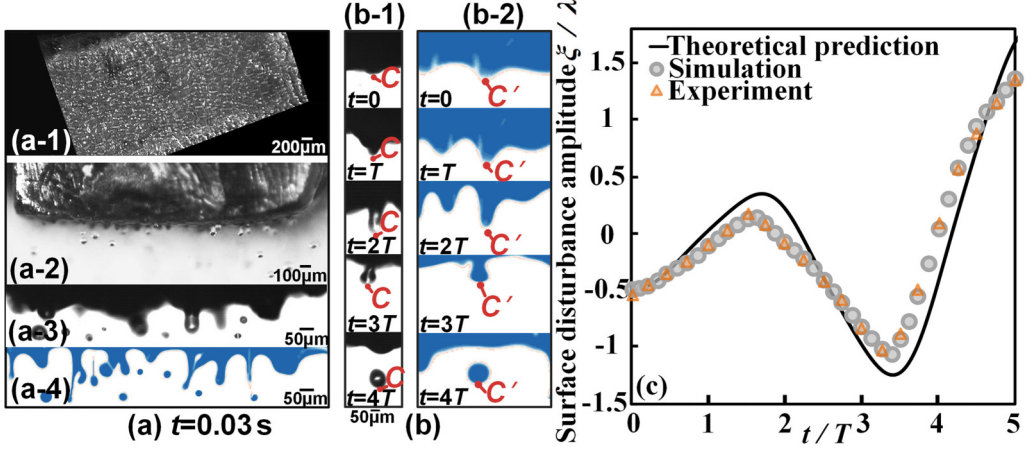


FIG. 5. (a) Faraday wave image at $t = 0.03$ s. (b) Droplet formation process in the experiment (b-1) and simulation (b-2). (c) Evolution of the perturbation displacement of the Faraday wave according to the theory, experiment, and simulation. The horizontal and vertical coordinates are the same as in Fig. 4(c). The detailed photographic parameters and displacement measurements are in Appendix A.

and

$$q^* = \frac{2(\rho_1 - \rho_2)kA_0}{\omega^2(\rho_1 + \rho_2)} = \frac{2(\rho_1 - \rho_2)k\Delta_0}{\rho_1 + \rho_2}, \quad (20)$$

where a^* and q^* represent the dimensionless forms of a and q ; $\Delta_0 = A_0/\omega^2$ represents the oscillation amplitude. Figure 6(a) shows the stability chart derived from Eq. (18) using the harmonic balance method [2].

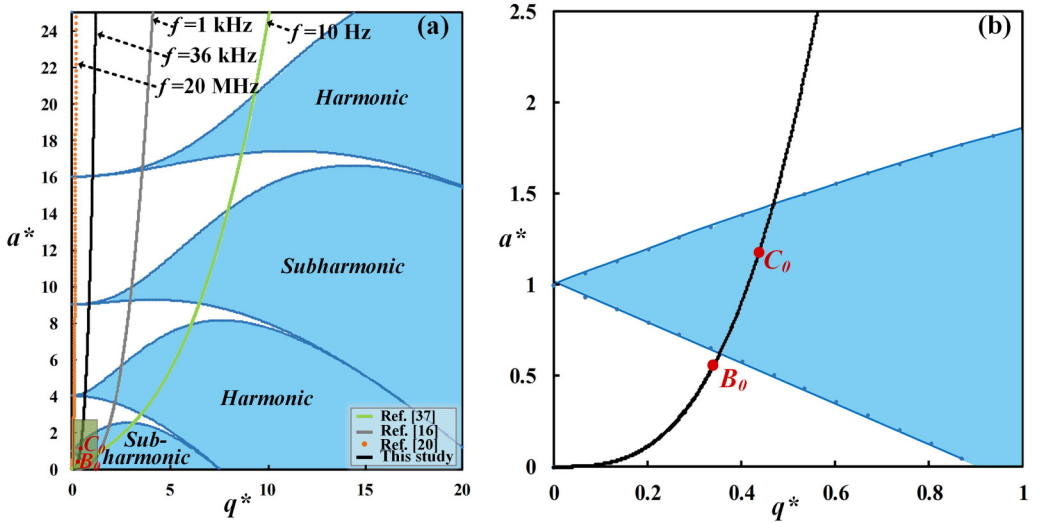


FIG. 6. (a) The first four orders of Faraday instability diagram in the (a^*, q^*) plane (blue shaded area: unstable region; white area: stable region). The four parameter curves correspond to the four different vibration devices. Points B_0 and C_0 represent parameter pairs under specific experimental conditions, and enlarged views of these two points are shown in (b).

We combine Eqs. (15) and (16) by eliminating the wave number k ,

$$a^* = \frac{\sigma(\rho_1 + \rho_2)^2}{2(\rho_1 - \rho_2)^3 \Delta_0^3 \omega^2} q^{*3} + \frac{2g}{\Delta_0 \omega^2} q^*, \quad (21)$$

where $\sigma(\rho_1 + \rho_2)^2/(\rho_1 - \rho_2)^3 \Delta_0^3 \omega^2$ and $g/\Delta_0 \omega^2$ are two dimensionless parameters related to actual experimental conditions. A cubic parameter curve for the given values of $\sigma(\rho_1 + \rho_2)^2/(\rho_1 - \rho_2)^3 \Delta_0^3 \omega^2$ and $g/\Delta_0 \omega^2$ can be drawn in the (a^*, q^*) plane [as shown in Fig. 3(a)], and the corresponding parameter pair (a^*, q^*) lies on this curve.

Using Eq. (21), we plotted the corresponding parameter curves for Figs. 4 and 5 in Fig. 6(a). The rising rate of the parameter curves is large and hardly crosses the unstable tongue except for the first-order unstable tongue [enlarged plot in Fig. 6(b)]. Therefore, only the subharmonics are excited, which is consistent with the experimental and simulation results. Unlike low-frequency oscillators, for high-frequency oscillators, Faraday waves consist mainly of low-order harmonics, and it is difficult to observe combinations of harmonics at different frequencies [35,36]. To explain this, we plotted in Fig. 6(a) the parameter curves in the experiments of Okada and Okada [37], Li *et al.* [16], and Qi *et al.* [20] corresponding to vibration frequencies of 10 Hz, 1.4 kHz, and 20 MHz; amplitudes of 810 μm , 137 μm , and 10 nm; and corresponding ρ_1 and ρ_2 of 998.2 and 1.3 kg/m^3 . When $f = 10$ Hz, the parameter curves rise slowly through the unstable tongues of different orders, resulting in Faraday waves of different frequencies being excited simultaneously and competing with each other, with the competitiveness depending on the line segment length of the parameter curve located within the unstable tongue. As the vibration frequency increases, the parameter curve gradually tilts closer to the a^* axis and the number of unstable tongues crossed decreases, leading to difficulties in exciting Faraday waves of different frequencies.

In the experiment, the average wavelengths of the steady-state and non-steady-state Faraday waves are 135 and 101 μm , respectively. According to the relationship between wavelength and wave number, and Eqs. (20) and (21), two parameter pairs (a^*, q^*) can be obtained, corresponding to point B_0 (0.344, 0.575) and point C_0 (0.46, 1.367) on the parameter curve, as shown in Figs. 6(a) and 6(b). Point B_0 is located in the stable region and point C_0 is located in the subharmonic instability region. Based on the linear theory [2], the surface perturbation displacements of point B_0 and point C_0 can be obtained, as shown in Figs. 4(c) and 5(c). For point B_0 , the perturbation displacement varies with time in an approximate sinusoidal function form and the perturbation period is twice the vibration period. The perturbation trajectory corresponding to point C_0 grows nonlinearly after a small oscillation, indicating that nonlinear effects start to become important. Compared to the experimental and simulated results, the theoretical predictions show larger displacement peaks and faster growth or decline because we completely ignore viscosity in the linear theoretical analysis, while in the experiments and simulations, the viscosity of the water slightly suppresses the surface perturbations. As a whole, the theoretical, simulated, and experimental results are in high agreement, indicating that it is feasible to study Faraday wave instability in ultrasonic atomization using parametric curve equations and simulation methods.

It is worth stating that in our previous studies, we observed that the droplet generation is related to the cavitation mechanism in addition to the surface wave mechanism [22]. However, in the present study, we did not observe cavitation. This is because the liquid volume in the present study is at the microliter level, which is much smaller than in previous studies (milliliter level), and the atomization time is greatly reduced, resulting in the formation and rupture of bubbles inside the liquid in time. Therefore, in this study, we do not consider the effect of cavitation on the atomization mechanism.

B. Viscous case

In the following, we consider the viscous dissipation, which is closer to the actual experimental conditions. Studying the recurrence, Eq. (16), with damping term β and setting the value of the

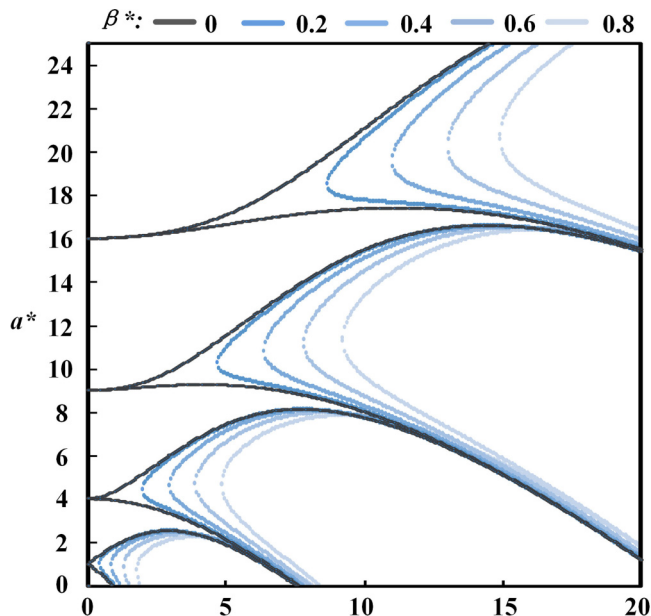


FIG. 7. The neutral stability boundary corresponding to different damping terms β in the (a^*, q^*) plane.

growth rate γ^* to 0, we can obtain the following dimensionless form equation:

$$q^* \xi_{n-1} + [4(\alpha^* + n)^2 + 4\beta^*(\alpha^* + n)] \xi_n + q^* \xi_{n+1} = a^* \xi_n, \quad n = 0, 1, 2, \dots, \quad (22)$$

where β^* represent the dimensionless forms of β . This equation can be rewritten as a generalized eigenvalue problem:

$$\mathbf{K}\xi = a\xi. \quad (23)$$

Selecting the smallest, real positive eigenvalues a , the neutral stable boundaries for different β^* values (0, 0.2, 0.4, 0.6, 0.8) in the (a^*, q^*) plane can be obtained as shown in Fig. 7. It is seen that as the value of β^* increases, the unstable tongues gradually moves away from the a^* axis. The unstable tongues' vertices become smooth and the area of instability shrinks.

Similar to the inviscid case, the Faraday instability in the viscous case is also determined by the position of the parameter pair in the instability diagram. From Eqs. (12) and (13), the parameter pair (a, q) is related to the experimental parameters (σ, ρ, Δ_0) and the wave number k . The unstable tongue is determined by the value of β , which is related to the viscosity η and the wave number k according to Eq. (11). Thus, in the viscous case, the Faraday instability depends on the experimental parameters (σ, ρ, Δ_0) , viscosity η , and wave number k . In this section, to exclude the interference of the experimental parameters (σ, ρ, Δ_0) , we fix their values and focus on the effect of wave number k and viscosity η on the Faraday instability. Since the instability modes of Faraday waves become very complicated under damped conditions, it is difficult to obtain an easily understandable parameter curve to study them quantitatively; therefore, we only perform a qualitative analysis.

First, assume that the Faraday wave number k is constant. As the viscosity η increases, the damping term β increases, and the corresponding unstable region gradually contracts. Therefore, the parameter pair may exit the unstable tongue, leading to a gradual stabilization of the Faraday wave. Since the higher-order unstable tongue contracts more than the lower-order unstable tongue, the parameter pairs have a higher probability of exiting and the higher-order unstable Faraday waves have a lower probability of being excited.

When the viscosity η is kept constant and k changes, both the parameter pair and the damping term change with k , and accordingly, the positions of the parameter pair and the instability tongue change. Specifically, when k becomes larger, both a and q increase, so the corresponding position of the parameter pair (a, q) in the instability diagram moves up to the right. The damping term β increases as k increases, and the corresponding first-order unstable tongue contracts to the lower right, while the other higher-order unstable tongues contract to the upper right. Therefore, the probability of Faraday wave instability evolution of the first order decreases, while the probability of Faraday wave instability evolution in the other higher-order unstable tongues depends on the moving speed of the parameter pair and the unstable tongue. When the parameter pair moves faster, the Faraday wave instability evolution can still be maintained. When the unstable tongue moves faster, the parameter pair will exit the unstable tongue and enter the stable tongue, which means that the Faraday wave instability evolution will stop and shift to the stable state.

When the viscosity η and k are changed simultaneously, both the parameter pair (a, q) and the damping term β change. Specifically, when the viscosity η and k increase or decrease simultaneously, the parameter pair (a, q) and the damping term β also increase or decrease simultaneously, so the corresponding parameter pair (a, q) and the position of the unstable tongue change in the same pattern as when k changes alone (the previous paragraph). However, when η and k change with different trends, the parameter pair (a, q) has the same trend as that of k , while the damping term β depends on η and k . This leads to uncertainty about the parameter pair (a, q) position in the instability diagram. In this case, the specific values of η and k need to be determined to analyze the Faraday instability.

VI. PARAMETER INFLUENCE MECHANISM OF ATOMIZATION CHARACTERISTICS

In the previous section, we verified that the parameter curves derived from the instability theory can accurately determine whether the Faraday wave is stable or not. However, in the practical application of ultrasonic atomization, it is not enough to judge whether the liquid can be atomized, but it is more important to optimize the atomization characteristics by controlling the parameters because the atomization characteristics directly determine the cost and product quality. Atomization characteristics mainly include atomization time and droplet size; the former reflects the efficiency and difficulty of atomization, while the latter can reflect the atomization performance. Therefore, we try to illustrate the effects of different parameters on the atomization characteristics by using parameter curves. Considering the inviscid case first, Eq. (16) can then be rewritten in the dimensionless form:

$$(4\delta^{*2} + a^*)\xi_n = q^*(\xi_{n+1} + \xi_{n-1}), \quad (24)$$

where $\delta^* = \delta/\omega$, and the real part γ^* of it represents the dimensionless growth rate of Faraday waves. We numerically solve the eigenvalues of Eq. (24) at different dimensionless growth rates γ^* (0.1, 0.3, 0.5, 0.7, 0.9), and then draw the instability curve on the $(a^* - q^*)$ plane, as shown in Fig. 8(a). The black curve plotted when the growth rate γ^* is zero indicates neutral instability. When the perturbation growth rate γ^* increases, it means that the Faraday instability intensity becomes larger and the envelope region of the unstable tongue gradually contracts to the right. The higher the order of the Faraday instability mode, the more obvious this contraction effect is. The parameter curves at different parameters correspond to different perturbation growth rates, which means that the Faraday wave instability intensity is different, which determines the atomization characteristics. Therefore, the change of atomization characteristics can be predicted by studying the change of parameter curves under different parameters. In the following, we will make theoretical predictions of the effects of amplitude, frequency, liquid surface tension, density, and liquid layer depth on the parameter curves in the inviscid case, and perform simulations and experimental verification of the atomization characteristics to gain insight into the parameter influence mechanism and provide theoretical guidance for the practical atomization.

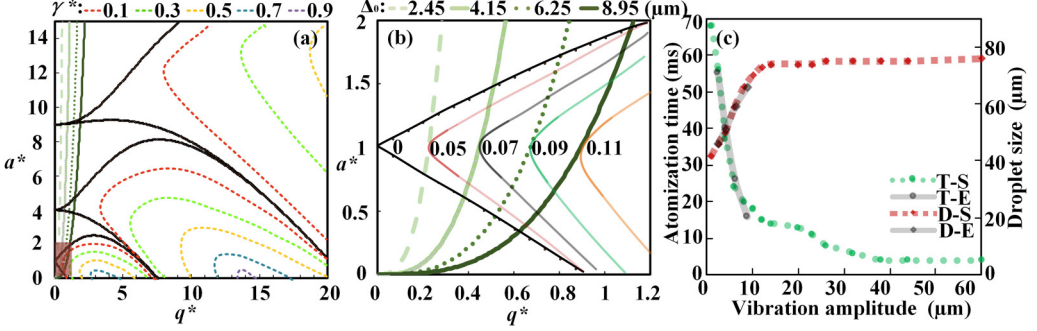


FIG. 8. (a) Instability tongue corresponding to different perturbation growth rates γ^* and parameter curves corresponding to different amplitudes Δ_0 . (b) Effect of amplitude Δ_0 on the maximum perturbation growth rate γ^* [enlarged view of the red shaded area in (a)]. (c) Atomization time and droplet size corresponding to different amplitudes Δ_0 . (*T-S* and *T-E* represent the atomization time in simulation and experiment, respectively, and *D-S* and *D-E* represent the droplet size in simulation and experiment, respectively.)

A. Vibration amplitude

First, we study the parameter curves and the corresponding maximum perturbation growth rates for different amplitudes; the parameter values are shown in Table I (case A) and Fig. 8(a) illustrates the parameter curves. It can be seen that the perturbation growth rates corresponding to the parameter curves are larger in the low-order unstable tongue than in the high-order unstable tongue because the boundary line of the high-order unstable tongue is more contracted to the right. Therefore, the maximum perturbation growth rate is located in the first-order instability region. The enlarged plot of the parameter curve within the first-order instability region is shown in Fig. 8(b). The parameter curve is tangent to the unstable tongue and the tangent point represents the maximum perturbation growth rate. As the amplitude increases, the rise of the parameter curve starts to slow down, and the corresponding maximum perturbation growth rate and the length of the curve segment through the unstable region increase, which indicates a gradual increase in the liquid instability and a significant increase in the atomization probability. This is consistent with a previous study by

TABLE I. Theoretical, simulation, and experimental parameters conditions. Table II in Appendix A contains details on the physicochemical properties of the liquids. The first line of each case represents the parameter values in experiment and theory, and the second line (in parentheses) represents the parameter values in simulation.

Cases	Liquid	f/kHz	$\Delta_0(\mu\text{m})$	$h(\mu\text{m})$
A	Water ($\sigma : 0.0727; \eta : 1.002; \rho_1 : 1000$)	36 (36)	2.45, 4.15, 6.25, 8.95 (1–60)	100 (100)
B	Water ($\sigma : 0.0727; \eta : 1.002; \rho_1 : 1000$)	36, 54, 60, 80 (20–200)	4.15 (4.15)	100 (100)
C	2%A, 5%A, 15%A, 75%A ($\sigma : 0.01\text{--}0.5, \eta : 1.002, \rho : 1000$)	36 (36)	6.25 (6.25)	100 (100)
D	($\sigma : 0.0727, \eta : 1.002, \rho_1 : 1000\text{--}2500$) ($\sigma : 0.0727; \eta : 1.002; \rho_1 : 100\text{--}10000$)	36 (36)	6.25 (6.25)	100 (100)
E	20%G, 30%G, 40%G, 50%G, 60%G ($\sigma : 0.0727, \eta : 1\text{--}11, \rho_1 : 100\text{--}10\,000$)	36 (36)	8.95 (8.95)	100 (100)
F	Water ($\sigma : 0.0727; \eta : 1.002; \rho_1 : 1000$)	36 (36)	6.25 (6.25)	10–200 (10–200)

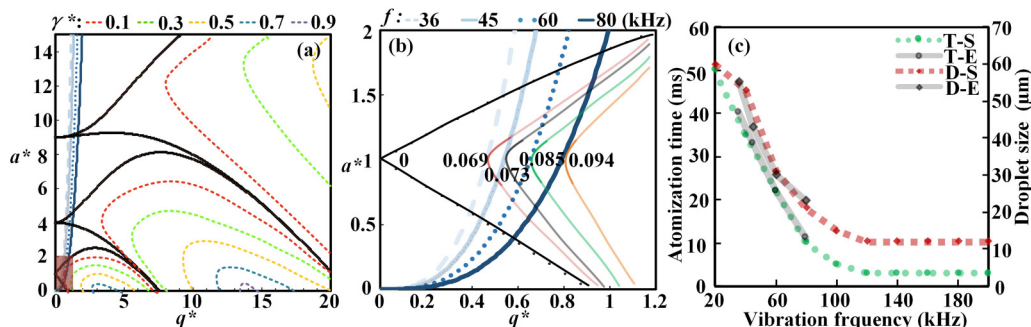


FIG. 9. (a) Instability tongue corresponding to different perturbation growth rates γ^* and parameter curves for different frequencies f . (b) The maximum perturbation growth rate corresponding to different frequencies f , and (b) is an enlarged view of the red shaded area in (a). (c) Atomization time and droplet size corresponding to different frequencies f . ($T-S$ and $T-E$ represent the atomization time in simulation and experiment, respectively, and $D-S$ and $D-E$ represent the droplet size in simulation and experiment, respectively.)

Liu *et al.* [16], who found that the larger the vibration acceleration amplitude, the easier the droplet is to atomize. Moreover, the value of q^* intersecting the instability curve gradually increases when the amplitude increases. According to Eq. (20), the increase of q^* here may be caused by the increase of the vibration amplitude, and we cannot tell whether the Faraday wave number k also increases.

To verify the theoretical predictions, we investigated the effect of amplitude on the atomization time and droplet size through experiments and simulations, as shown in Fig. 8(c). Considering the time cost of the simulation, the atomization time is defined as the time experienced by the liquid layer from rest to the atomization start, which represents the difficulty of atomization. To compensate for the limited choice of parameters in the experiments, the parameter range is extended in the simulations. As the amplitude increases, the energy transfer efficiency from the vibrating head to the liquid increases and the unstable evolution of the Faraday wave becomes faster, leading to shorter atomization time and lower atomization difficulty, which is consistent with the theoretical prediction. In the simulation, the atomization time decreases to 4 ms when the amplitude increases to 38 μm , after which the atomization time no longer decreases with increasing amplitude, indicating that there is a lower limit to the atomization time decrease. This is because the liquid needs some time to absorb enough mechanical energy to generate Faraday waves. In the experiments, the droplet size gradually increases with increasing amplitude, which is consistent with the results of Peskin and Raco [38]. In the simulations, the droplet size first increases and then remains constant as the amplitude continues to increase. The increase in amplitude causes some liquid to be thrown out directly before the Faraday wave is generated, resulting in some large droplets. However, there is an upper limit to this effect, which is due to the increase in energy transfer efficiency, which causes some of the liquid to reproduce Faraday waves, and therefore the droplets become larger at a reduced rate. This could explain the observation of Barreras *et al.* that droplet size is independent of amplitude [39]. Moreover, according to Lang [24], droplet size and Faraday wavelength are positively correlated, while wavelength is inversely proportional to wave number ($k = 2\pi/\lambda$). Therefore, as the amplitude increases, the wave number first decreases and then remains constant, which fills the gap in the theoretical prediction.

B. Vibration frequency

Figure 9 shows the effect of vibration frequency on Faraday instability, and the corresponding parameter values are shown in Table I (case B). The maximum perturbation growth rate is still located in the first-order instability region [Fig. 9(a)], and both the perturbation growth rate and the length of the parameter curve located in the instability region increase with the increased vibration

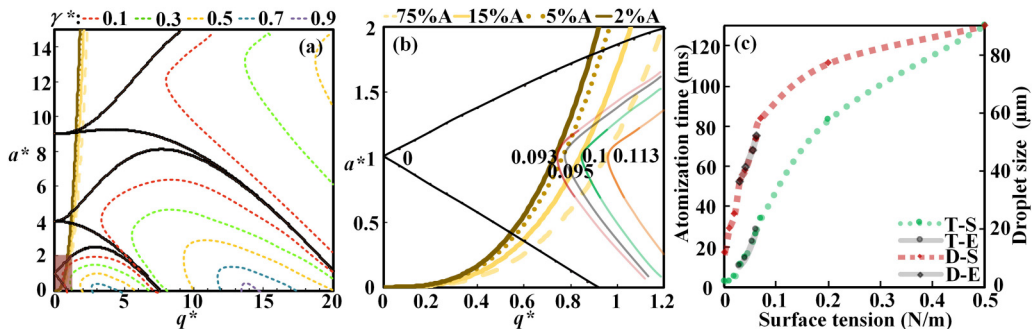


FIG. 10. (a) The instability tongue corresponding to different perturbation growth rates γ^* and the parameter curves corresponding to different surface tensions σ . (b) Effect of surface tension σ on the maximum perturbation growth rate; (b) is a magnified view of the red shaded area in (a). (c) Atomization time and droplet size corresponding to different surface tension σ . (*T-S* and *T-E* represent the atomization time in simulation and experiment, respectively, and *D-S* and *D-E* represent the droplet size in simulation and experiment, respectively.)

frequency [Fig. 9(b)]. This indicates that the higher the vibration frequency, the more unstable the excited Faraday waves are and the more easily atomization occurs. In addition, the value of q^* corresponding to the intersection of the parameter curve with the neutral stability boundary increases with the increased vibration frequency. According to Eq. (20), the wave number k increases and, therefore, the corresponding wavelength and droplet size decrease.

Figure 9(c) shows the effect of vibration frequency on the atomization characteristics in the experiments and simulations. In the experiments, the atomization time decreases with increasing vibration frequency, indicating that atomization occurs faster and atomization becomes progressively easier. The droplet size also decreases with increasing vibration frequency, which is consistent with the theoretical prediction. In the simulations, the atomization time and droplet size decrease to a minimum when the vibration frequency increases to 120 kHz and then remain constant, indicating that a minimum droplet size exists as well as the atomization time. The decrease in droplet size implies an increase in surface energy, and when the input energy is constant, the transformed surface energy is finite according to energy conservation, so the droplet size cannot be reduced indefinitely.

C. Surface tension

Figures 10(a) and 10(b) show the effect of the liquid surface tension on the parameter curves and the maximum perturbation growth rate, and the parameter values are shown in Table I (case C). As the surface tension increases, the parameter curve gradually shifts in the negative direction of the q^* axis, the length of the curve segment located in the instability region decreases, and the corresponding maximum growth rate decreases. This indicates that the increase in surface tension reduces the Faraday instability and makes atomization difficult. In addition, the value of q^* corresponding to the intersection of the parameter curve with the neutral stability line decreases with the increasing surface tension. According to Eq. (20), the Faraday wave number k decreases, which leads to an increase in wavelength and droplet size.

With the same parameters, we experimentally verified the theoretical predictions, as shown in Fig. 10(c). The atomization time increases with the increasing surface tension, indicating that the surface tension inhibits the liquid perturbation, leading to a significant decrease in the atomization speed and an increase in the atomization difficulty. This is because the increased surface tension leads to an increase in the liquid surface binding and the formation of Faraday waves becomes difficult. In addition, the droplet size increases with the increasing surface tension. When the input

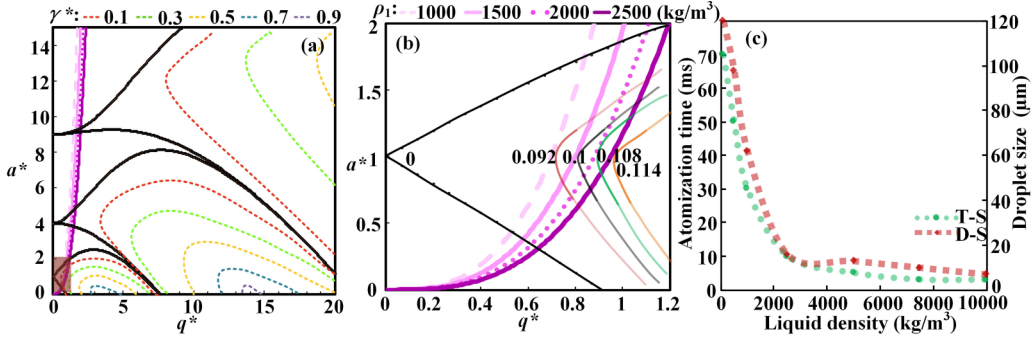


FIG. 11. (a) Instability tongue corresponding to different perturbation growth rates γ^* and parameter curves corresponding to different liquid densities ρ_1 . (b) The effect of liquid density ρ_1 on the maximum perturbation growth rate; (b) is a zoomed-in view of the red shaded area in (a). (c) Atomization time ($T-S$) and droplet size ($D-S$) corresponding to different liquid densities ρ_1 in the simulation.

energy is unchanged, the liquid tends to produce larger droplets to maintain the total surface energy constant. Under the simulated conditions, both atomization time and droplet size increase with increasing surface tension, but the growth rate becomes progressively slower, which is consistent with the theoretical results. From Fig. 10(b), the shift of the parameter curve toward the negative direction of the q^* axis becomes smaller as the surface tension increases, implying that the reduction of the perturbation growth rate also becomes smaller, which indicates that the inhibitory effect of surface tension on the Faraday instability gradually becomes less pronounced. This could explain the negligible effect of surface tension found by Lioubashevski in his experiments [40].

D. Density

Next, we will study the effect of liquid density on Faraday instability. Before the discussion, some clarifications are needed: First, in this paper, we only discuss the effect of liquid density on Faraday instability and ignore the effect of gas density. This is because the gas density is much smaller compared to the liquid density and does not have a large range of variation. Therefore, the variation of gas density has little effect on the values of $(\rho_1 + \rho_2)$ and $(\rho_1 - \rho_2)$ in the expression of the parameter curve [Eq. (21)]; it can be inferred that the effect of gas density on Faraday instability is also very weak. Second, it is difficult to find a set of liquids in which only the density changes with little difference in surface tension and viscosity; therefore, it is difficult to conduct validation experiments. Considering the limitations of experimental conditions, the theoretical predictions are verified by simulations only.

The parameters chosen in the theoretical predictions are shown in Table I (case D) and the results are presented in Figs. 11(a) and 11(b). As the liquid density increases, the parameter curve slopes in the positive direction of the q^* axis, which leads to an increase in both the length of the curve segments located within the instability region and the perturbation growth rate. This indicates that the increasing liquid density favors the Faraday instability, leading to a decrease in atomization difficulty. It can be inferred that the atomization time will decrease as the liquid density increases. Moreover, as the liquid density increases, the intersection of the parameter curve with the instability tongue shifts to the right, corresponding to larger values of q^* [Fig. 11(b)]. According to the expression (20), the Faraday wave number increases, so the wavelength becomes shorter and the average droplet size decreases. The above changes in both atomization time and droplet size were verified in the simulation, as shown in Fig. 11(c). When the liquid density increases while the gas density remains constant, the resistance to liquid morphology changes decreases, atomization becomes easier, and therefore more Faraday waves are generated and droplet size

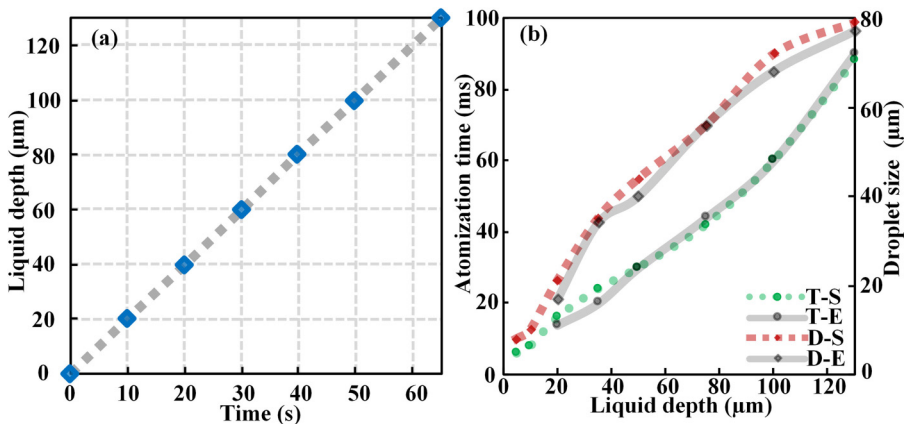


FIG. 12. (a) The relationship between liquid depth and liquid supply time. (b) Atomization time and droplet size corresponding to different liquid depths h . (T - S and T - E represent the atomization time in simulation and experiment, respectively, and D - S and D - E represent the droplet size in simulation and experiment, respectively.)

decreases. However, there is a lower limit for both the reduction in atomization time and droplet size.

E. Liquid depth

In deriving the Mathieu equation [Eq. (10)], we assumed $\tanh kh \rightarrow 1$ and thus neglected the effect of liquid depth on Faraday instability. However, in the experiments, we found that the atomization characteristics change when the liquid depth is varied. The liquid depth is positively correlated with the liquid supply time [Fig. 12(a)]. When the liquid supply time is increased to 65 s, the liquid layer depth is 130 μm . When we continue to increase the liquid supply time, the liquid surface becomes curved due to surface tension and gravity, which do not match the characteristics of the horizontal liquid film in this study, and therefore, it is out of our scope to study a larger depth. We simulated the effect of liquid depth on the atomization characteristics, and the parameters were selected as shown in Table I (case E), and the results are shown in Fig. 12(b). In the simulation, the maximum liquid depth is set to 130 μm . As the liquid depth increases, the energy transfer to the liquid surface becomes slower, which decelerates the liquid surface deformation and therefore the atomization time becomes longer. The surface energy of the liquid increases with the liquid depth, and when the energy input to the system is kept constant, the liquid tends to produce larger droplets to balance the energy output with the input. We conducted experiments to verify the simulation results [Fig. 12(b)], and both results agree well. The experimental and simulation studies fill a gap in the theoretical study.

F. Viscosity

When the viscous case is considered, the parameter curves and the perturbation growth rate theory of the nonviscous case are no longer applicable. For the viscous case, at the apex of each unstable tongue, there is a pair of instability thresholds (a_c^* , q_c^*) (Fig. 7) representing the minimum vibration amplitude required for the Faraday wave instability, which can reflect the atomization difficulty. Therefore, the effect of damping β^* on the thresholds a_c^* and q_c^* reflects the effect of viscosity on the Faraday instability. The thresholds a_c^* and q_c^* for different β^* are shown in Fig. 13. For the first-order unstable tongue ($l = 1$), a_c^* decreases with increasing viscosity effect, while for the other higher-order unstable tongues, a_c^* increases with increasing β^* [Fig. 13(a)]. For ultrasonic

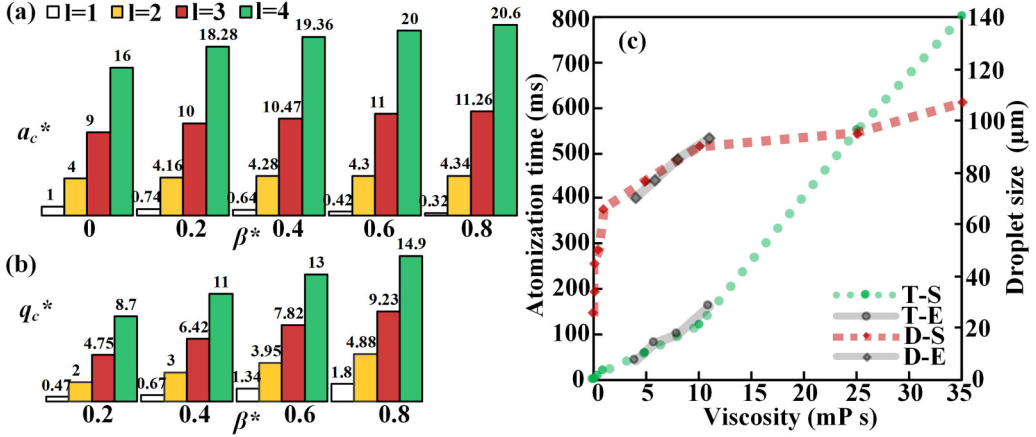


FIG. 13. Instability thresholds (a) a_c^* and (b) q_c^* corresponding to different damping terms β^* and orders l . (c) Atomization time and droplet size corresponding to different liquid viscosities η . (T - S and T - E represent the atomization time in simulation and experiment, respectively, and D - S and D - E represent the droplet size in simulation and experiment, respectively.)

atomization, since Faraday instability occurs mainly in the first-order instability region, the variation of the threshold a_c^* within the first-order instability tongue is the focus of our attention. According to Eq. (12), a decrease in a_c^* indicates a decrease in the corresponding Faraday wave number; therefore, the wavelength and average droplet size increase accordingly. As the damping term β^* increases, q_c^* gradually moves away from the a_c^* axis, leading to an increase in the corresponding amplitude [Fig. 13(b)] and, therefore, an increase in atomization difficulty. In addition, the value of q_c^* increases when the order l of the unstable tongue increases [Fig. 13(b)]. This indicates that the amplitude required to excite the higher-order Faraday instability is larger. Therefore, for viscous liquids, it is difficult to observe higher-order Faraday waves in practical atomization experiments [41].

To verify the theoretical predictions, experiments and simulations were performed with the parameters shown in Table I (case F), and the results are presented in Fig. 13(c). The increase in atomization time with increasing viscosity indicates that viscosity acts as a hindrance to the liquid perturbation, slowing down the Faraday instability evolution and increasing the atomization difficulty. This is because the viscous dissipation becomes more and the liquid needs more time to absorb energy to overcome the viscous forces. The average droplet size grows with increasing viscosity and the growth rate becomes progressively slower (in the simulation). This is because as the atomization time increases, the liquid input energy becomes progressively more and the translatable surface energy increases, slowing down the growth of droplet size.

Furthermore, the forced resonance frequency of the Faraday wave affected by the viscous damping effect deviates compared to the resonance condition without the viscous damping term [42]. We denote this deviation as $a_{l,\beta}$, where $a_{l,\beta}$ refers to the difference between the values of a_c^* corresponding to large and small damping in an unstable tongue of order l . The resonance condition for a viscous system can be written as

$$\Omega = \frac{1}{2}(l^2 + a_{l,\beta})^{1/2}\omega. \quad (25)$$

Since the value of $a_{l,\beta}$ in the first-order unstable tongue is negative, the first-order forced resonant frequency ω in the viscous case is slightly higher than that in the nonviscous case for the same excitation vibration frequency Ω , while the other higher-order unstable tongues have positive $a_{l,\beta}$ values, and accordingly, the forced resonant frequency ω in the viscous case is lower than that in the nonviscous case.

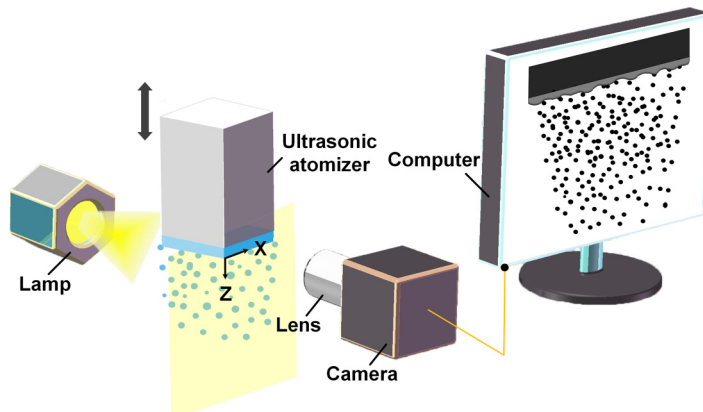


FIG. 14. Ultrasonic atomization photography system.

VII. CONCLUSIONS

In this study, the evolution mechanism of Faraday instability in ultrasonic atomization and the mechanism of parameter effects on atomization characteristics are explained by three methods: theoretical, experimental, and simulation. The main conclusions drawn are as follows.

Using the instability theory under inviscid conditions, the parameter curve equation is derived. The appearance of harmonics at different frequencies depends mainly on the vibration frequency. The parameter curve of the high-frequency atomizer is steeper compared to that of the low-frequency atomizer, leading to always excited subharmonics. The simulation results of multiple Faraday wave evolution are in high agreement with the experimental results. In both experiments and simulations, stable and unstable Faraday waves correspond to parameter pairs located outside and inside the unstable tongue, corresponding to linear and nonlinear states. The liquid surface perturbation displacement evolution is plotted based on linear theory, experiments, and simulations, and the three are in good agreement. In the viscous case, the evolution of the Faraday instability depends on the wave number and viscosity.

The intensity of the Faraday instability depends on the maximum perturbation growth rate and the instability threshold in the inviscid and viscous cases, respectively. When the vibration frequency and liquid density increase while the liquid surface tension, depth, and viscosity decrease, the Faraday instability is enhanced, and the atomization time and droplet size decrease. When the amplitude increases, Faraday instability increases, atomization time decreases, and droplet size increases.

All the theoretical predictions in this study were validated by experiments and simulations, which can guide the practical application of ultrasonic atomization.

ACKNOWLEDGMENT

We would like to thank Prof. Yikai Li and Dr. N. Kang for their strong support and suggestions in our research work.

APPENDIX A: MEASUREMENT METHODS AND MATERIALS

Figure 14 shows the photographic system used for the atomization process, including a high-speed camera (Photron FASTCAM Mini UX100, Japan), a lens, a computer, and a lamp. To obtain highly representative atomization images, the symmetrical surface of the vibrating head was chosen as the focal plane. According to different needs, two lenses were configured in the experiment: a Navitar Zoom 6000 (maximum optical magnification: $6.3\times$; focal length: 33 mm) and a Leica

TABLE II. Physicochemical properties of liquids.

Solution	Mass fraction	Surface tension σ (mN/m)	Viscosity η (mP s)	Density ρ (kg/m ³)
Water	–	72.75	1.002	998.2
Glycerol	20%	41.6	4	1117.1
	30%	41	5.76	1136.4
	40%	40.8	7.98	1150
	50%	40.3	11	1189.7
	60%	40.1	31	1198.4
Alcohol	2%	63.37	1.47	988.7
	5%	55.21	1.4	976.4
	15%	41.87	1.41	966.3
	75%	29	1.43	954.2

APO Tele Elmar-S (maximum optical magnification: $10\times$; focal length: 20 mm), which were used to capture atomization scenes with large and small fields of view, respectively. The computer is connected to the high-speed camera to display the captured images in real time. To obtain a clearer atomization scene, the backlight photography method was used in the experiment. The light and the camera are placed behind and in front of the atomizer, respectively, and the three are adjusted in a straight line and the distances between them are changed to contrast the atomized scene and the surrounding background as much as possible.

The photographic parameters of Figs. 4 and 5 are as follows: Figs. 4(a-1) and 5(a-1) represent the elevation view of the vibration head with the photographic parameters: Navitar Zoom 6000 lens, fps = 12 500, shutter speed = 1 s^{-1} ; Figs. 4(a-2) and 5(a-2) are the front view of the vibration head with a magnification of $4\times$. The photographic parameters are Navitar Zoom 6000 lens, fps = 4000, shutter speed = 1 s^{-1} . Figures 4(a-3) and 5(a-3) are Faraday wave diagrams with a magnification of $10\times$. The photographic parameters are lens Leica APO Tele Elmar-S, fps = 200 000, and shutter speed = $25\text{ }\mu\text{s}^{-1}$.

In the experiments, the displacements of point *B* (Fig. 4) and point *C* (Fig. 5) were measured by calibrating specific points on the continuously taken pictures using the PHOTRON FASTCAM VIEWER, an image processing software for high-speed CCDs, and then using the ruler tool for displacement measurement. In the simulation, the displacements of point *B'* (Fig. 4) and point *C'* (Fig. 5) were measured by the postprocessing software TECPLOT. For the experiments and simulations, the displacement measurements were performed at intervals of $1/4 T$ and $1/8 T$, respectively, with no less than five different sample points selected for each measurement. Figures 4(c) and 5(c) show the average displacement values in the experiments and simulations.

The droplet size was measured with a Malvern laser particle sizer (UK). A schematic diagram and detailed description of the droplet size measurement system can be found in our previous paper [22]. In the simulation, the average diameter measurement was performed after automatically identifying and depicting the droplets by IMAGE PRO PLUS (IPP) image analysis software. The droplet size in this paper represents the average values, and each set of measurements was repeated no less than five times. The droplet size is approximately normally distributed with a standard deviation of no more than 30% of the mean droplet size.

In this experiment, de-ionized water, different concentrations of alcohol solutions, and glycerol solutions were chosen to study the effect of physical and chemical properties of liquids on Faraday instability. The physicochemical properties of the solutions are shown in Table II. It can be seen that the differences in density and viscosity of different concentrations of alcohol solution are very weak, while the differences in density and surface tension of different concentrations of glycerol solution are also not significant. Therefore, the effect of liquid surface tension and viscosity on the

Faraday instability can be studied with the alcohol solution and the glycerol solution, respectively. For convenience, alcohol solutions with concentrations of 2%, 5%, 15%, and 75% are abbreviated as 2%A, 5%A, 15%A, and 75%A. The surface tension of the alcohol solutions increased as the alcohol concentration increased. Glycerol solutions with concentrations of 20%, 30%, 40%, 50%, and 60% are abbreviated as 20%G, 30%G, 40%G, 50%G, and 60%G. The viscosity of glycerol solutions increases with increasing glycerol concentration.

APPENDIX B: MATRIX \mathbf{K}

The matrix \mathbf{K} in Eq. (26) is as follows:

$$\mathbf{K} = \begin{bmatrix} 0 & 0 & 2q & 0 & 0 & 0 & \dots \\ 0 & 0 & 0 & 0 & 0 & 0 & \dots \\ q & 0 & 4 & 4\beta & q & 0 & \dots \\ 0 & q & -4\beta & 4 & 0 & q & \dots \\ 0 & 0 & q & 0 & 16 & 8\beta & \dots \\ 0 & 0 & 0 & q & -8\beta & 16 & \dots \\ \vdots & \vdots & \vdots & \vdots & \vdots & \vdots & \dots \end{bmatrix} \quad (\text{B1})$$

for the harmonic cases, and

$$\mathbf{K} = \begin{bmatrix} q+1 & 2\beta & 1 & 0 & 0 & 0 & \dots \\ -2\beta & -q+1 & q & 0 & 0 & 0 & \dots \\ q & 0 & 9 & 6\beta & q & 0 & \dots \\ 0 & q & -6\beta & 9 & 0 & q & \dots \\ 0 & 0 & q & 0 & 25 & 10\beta & \dots \\ 0 & 0 & 0 & q & -10\beta & 25 & \dots \\ \vdots & \vdots & \vdots & \vdots & \vdots & \vdots & \dots \end{bmatrix} \quad (\text{B2})$$

for the subharmonic cases.

-
- [1] M. Faraday, On a peculiar class of acoustical figures; and on certain forms assumed by groups of particles upon vibrating elastic surfaces, *Philos. Trans. R. Soc. London* **121**, 299 (1831).
 - [2] T. B. Benjamin and F. Ursell, The stability of the plane free surface of a liquid in vertical periodic motion, *Proc. R. Soc. London, Ser. A* **225**, 505 (1954).
 - [3] W. Eisenmenger, Dynamic properties of the surface tension of water and aqueous solutions of surface active agents with standing capillary waves in the frequency range from 10 kc/s to 1.5 Mc/s, *Acta Acust. Acust.* **9**, 327 (1959).
 - [4] S. Ciliberto and J. P. Gollub, Phenomenological model of chaotic mode competition in surface waves, *Nuovo Cimento D* **6**, 309 (1985).
 - [5] K. Kumar and L. S. Tuckerman, Parametric instability of the interface between two fluids, *J. Fluid Mech.* **279**, 49 (1994).
 - [6] K. Kumar, Linear theory of Faraday instability in viscous liquids, *Proc. R. Soc. A* **452**, 1113 (1996).
 - [7] W. Zhang and J. Viñals, Pattern formation in weakly damped parametric surface waves, *J. Fluid Mech.* **336**, 301 (1997).
 - [8] E. Bosch, H. Lambermont, and W. van de Water, Average patterns in Faraday waves, *Phys. Rev. E* **49**, R3580 (1994).
 - [9] A. V. Kityk, J. Embs, V. V. Mekhonoshin, and C. Wagner, Spatiotemporal characterization of interfacial Faraday waves by means of a light absorption technique, *Phys. Rev. E* **72**, 036209 (2005).
 - [10] B. Christiansen, P. Alstrøm, and M. T. Levinsen, Ordered Capillary-Wave States: Quasicrystals, Hexagons, and Radial Waves, *Phys. Rev. Lett.* **68**, 2157 (1992).

- [11] K. Kumar and K. M. S. Bajaj, Competing patterns in the Faraday experiment, *Phys. Rev. E* **52**, R4606 (1995).
- [12] N. Perinet, D. Juric, and L. S. Tuckerman, Numerical simulation of Faraday waves, *J. Fluid Mech.* **635**, 1 (2009).
- [13] N. Périnet, D. Juric, and L. S. Tuckerman, Alternating Hexagonal and Striped Patterns in Faraday Surface Waves, *Phys. Rev. Lett.* **109**, 164501 (2012).
- [14] Y. Li, M. Zhang, and K. Wu, Three-dimensional simulation of ligament formation and breakup caused by external vibration, *Phys. Fluids* **32**, 083605 (2020).
- [15] K. Takagi and T. Matsumoto, Numerical simulation of two-dimensional Faraday waves with phase-field modelling, *J. Fluid Mech.* **686**, 409 (2011).
- [16] F. Liu, N. Kang, and Y. Li, Experimental investigation on the atomization of a spherical droplet induced by Faraday instability, *Exp. Therm. Fluid Sci.* **100**, 311 (2019).
- [17] J. X. Wang, Y. Z. Li, J. X. Li, C. Li, Y. Zhang, and X. W. Ning, A gas-atomized spray cooling system integrated with an ejector loop: Ejector modeling and thermal performance analysis, *Energy Convers. Manage.* **180**, 106 (2019).
- [18] E. Assadpour, Y. Maghsoudlou, S. M. Jafari, M. Ghorbani, and M. Aalami, Optimization of folic acid nano-emulsification and encapsulation by maltodextrin whey protein double emulsions, *Int. J. Biol. Macromol.* **86**, 197 (2016).
- [19] M. Mezhericher, I. Ladizhensky, and I. Etlin, Atomization of liquids by disintegrating thin liquid films using gas jets, *Int. J. Multiphase Flow* **88**, 99 (2016).
- [20] A. Qi, J. R. Friend, L.Y. Yeo, D. A. V. Morton, M. P. McIntosh, and L. Spiccia, Miniature inhalation therapy platform using surface acoustic wave microfluidic atomization, *Lab Chip* **9**, 2184 (2009).
- [21] P. Deepu, C. Peng, and S. Moghaddam, Dynamics of ultrasonic atomization of droplets, *Exp. Therm. Fluid Sci.* **92**, 243 (2018).
- [22] Y. Zhang, S. Yuan, and L. Wang, Investigation of capillary wave, cavitation, and droplet diameter distribution during ultrasonic atomization, *Exp. Therm. Fluid Sci.* **120**, 110219 (2021).
- [23] R. W. Wood, A. L. Loomis, and L. Loomis, The physical and biological effects of high-frequency sound-waves of great intensity, *Philos. Mag. Series* **4**, 417 (1927).
- [24] R. J. Lang, Ultrasonic atomization of liquids, *J. Acoust. Soc. Am.* **34**, 6 (1962).
- [25] R. Rajan and A. B. Pandit, Correlations to predict droplet size in ultrasonic atomization, *Ultrasonics* **39**, 235 (2001).
- [26] E. D. Wilkes and O. A. Basaran, Forced oscillations of pendant (sessile) drops, *Phys. Fluids* **9**, 1512 (1997).
- [27] E. D. Wilkes and O. A. Basaran, Drop ejection from an oscillating rod, *Colloid Interface Sci.* **242**, 180 (2001).
- [28] Y. Li, P. Zhang, and N. Kang, Linear analysis on the interfacial instability of a spherical liquid droplet subject to a radial vibration, *Phys. Fluids* **30**, 10 (2018).
- [29] J. Liu, R. Ma, Y. Yuan, X. Yang, and W. Ma, Linear stability of a fluid mud–water interface under surface linear long travelling wave based on the floquet theory, *Eur. J. Mech., B: Fluids* **86**, 37 (2021).
- [30] S. Mukherjee and M. C. Rechtsman, Observation of Floquet solitons in a topological bandgap, *Science* **368**, 6493 (2020).
- [31] L. Kelvin, XLVI. Hydrokinetic solutions and observations, *London, Edinburgh Dublin Philos. Mag. J. Sci.* **42**, 362 (1871).
- [32] F. Liu, Y. Xu, and Y. Li, A coupled level-set and volume-of-fluid method for simulating axi-symmetric incompressible two-phase flows, *Appl. Math. Comput.* **293**, 112 (2017).
- [33] D. L. Sun and W. Q. Tao, A coupled volume-of-fluid and level set (VOSET) method for computing incompressible two-phase flows, *Int. J. Heat Mass Transfer* **53**, 645655 (2010).
- [34] B. M. Ningegowda and B. Premachandran, A coupled level set and volume of fluid method with multi-directional advection algorithms for two-phase flows with and without phase change, *Int. J. Heat Mass Transfer* **79**, 532 (2014).
- [35] H. Urra, J. F. Marín, M. Páez-Silva, M. Taki, S. Coulibaly, L. Gordillo and M. A. García-Ñustes, Localized Faraday patterns under heterogeneous parametric excitation, *Phys. Rev. E* **99**, 033115 (2019).

- [36] S. Zhao, M. Dietzel, and S. Hardt, Faraday instability of a liquid layer on a lubrication film, *J. Fluid Mech.* **879**, 44 (2019).
- [37] M. Okada and M. Okada, Observation of the shape of a water drop on an oscillating Teflon plate, *Exp. Fluids* **41**, 789 (2006).
- [38] R. L. Peskin and R. J. Raco, Ultrasonic atomization of liquids, *J. Acoust. Soc. Am.* **35**, 1378 (1963).
- [39] F. Barreras, H. Amaveda, and A. Lozano, Transient high-frequency ultrasonic water atomization, *Exp. Fluids* **33**, 405 (2002).
- [40] O. Lioubashevski, J. Fineberg, and L. S. Tuckerman, Scaling of the transition to parametrically driven surface waves in highly dissipative systems, *Phys. Rev. E* **55**, R3832(R) (1997).
- [41] K. A. Ramisetty, A. B. Pandit, and P. R. Gogate, Investigations into ultrasound induced atomization, *Ultrason. Sonochem.* **20**, 254 (2013).
- [42] J. Li, X. Li, and S. Liao, Stability and hysteresis of Faraday waves in Hele-Shaw cells, *J. Fluid Mech.* **871**, 711 (2019).